



Depth-extended, high-resolution fluorescence microscopy: whole-cell imaging with double-ring phase (DRiP) modulation

XUANWEN HUA,¹ CHANGLIANG GUO,¹ JIAN WANG,^{2,3} DEBORAH KIM-HOLZAPFEL,⁴ BRYCE SCHROEDER,^{2,5} WENHAO LIU,¹ JUNHUA YUAN,⁶ JARROD FRENCH,⁴ AND SHU JIA^{1,*}

¹Department of Biomedical Engineering, Georgia Institute of Technology and Emory University, Atlanta, Georgia 30332, USA

²Department of Biomedical Engineering, Stony Brook University, Stony Brook, New York 11794, USA

³Department of Physics, Harbin Institute of Technology, Harbin 150001, China

⁴Department of Biochemistry and Cell Biology and Department of Chemistry, Stony Brook University, Stony Brook, New York 11794, USA

⁵Medical Scientist Training Program, School of Medicine, Stony Brook University, Stony Brook, New York 11794, USA

⁶Department of Physics, University of Science and Technology of China, Hefei 230026, China

*shu.jia@gatech.edu

<https://sites.google.com/site/thejialab/>

Abstract: We report a depth-extended, high-resolution fluorescence microscopy system based on interfering Bessel beams generated with double-ring phase (DRiP) modulation. The DRiP method effectively suppresses the Bessel side lobes, exhibiting a high resolution of the main lobe throughout a four- to five-fold improved depth of focus (DOF), compared to conventional wide-field microscopy. We showed both theoretically and experimentally the generation and propagation of a DRiP point-spread function (DRiP-PSF) of the imaging system. We further developed an approach for creating an axially-uniform DRiP-PSF and successfully demonstrated diffraction-limited, depth-extended imaging of cellular structures. We expect the DRiP method to contribute to the fast-developing field of non-diffracting-beam-enabled optical microscopy and be useful for various types of imaging modalities.

© 2018 Optical Society of America under the terms of the [OSA Open Access Publishing Agreement](#)

1. Introduction

As a solution to the scalar Helmholtz equation, Bessel beams are a well-known type of non-diffracting beams that can propagate over many Rayleigh lengths without appreciable diffraction and are self-healing after being obscured in scattering media [1–3]. The simplest Bessel beam profile is described by a zeroth-order Bessel function of the first kind, which is composed of a narrow main lobe surrounded by a decaying set of side lobes [1,2]. The unique properties of Bessel beams have drawn broad interests in areas ranging from vectorial wave physics [4–7], to applications such as optical manipulation [8,9], micro-machining [10,11], spatiotemporal light shaping [12], and nonlinear optics [13], to the generation of varying Bessel waveforms, such as electron beams [14], plasmonic waves [15], acoustic waves [16] and quantum waves [17].

Amongst many applications, recent years have witnessed the emergence of non-diffracting-beam-enabled optical imaging [18–26]. Compared to the conventional methods using the standard Gaussian beams for illumination, Bessel beams effectively mitigate the trade-off between the axial Rayleigh length (i.e. the DOF) and the lateral beam width. The use of Bessel beams has significantly improved the imaging capabilities of optical microscopy, such as the field of view (FOV) for light-sheet illumination [18,20,24] and the scanning speed for two-photon microscopy [23,25]. In addition, the non-diffracting and self-healing features

of Bessel beams allow robust light propagation over a longer distance in highly heterogeneous biological specimens, effectively overcoming heterogeneity-induced distortions in deep-tissue imaging [19,21,22].

Although highly promising, the challenge for broader applications of Bessel beams remains due to the influence of Bessel side lobes [27]. While the side lobes are crucial for the non-diffracting and self-healing properties of the main lobe, their extended profiles contribute substantial out-of-focus background, leading to degraded image contrast and resolution. Existing methods to circumvent this limitation include two-photon excitation [18,25], structured illumination [18,28,29], and confocal line detection [30,31]. However, these methods induce complexity in instrumentation. Alternatively, several recent studies have demonstrated that the destructive interference between two harmonic cosine-Gaussian beams can largely suppress the side lobes without deteriorating the main lobe [32,33]. These methods allow for simplified system design while maintaining high controllability of the Bessel waveforms, thus implying a promising imaging scheme for Bessel-beam-facilitated optical microscopy.

We introduce here a DRiP method that enables depth-extended, high-resolution fluorescence microscopy using interfering Bessel beams. Compared to conventional wide-field microscopy, the method effectively suppresses the Bessel side lobes, exhibiting a high resolution of the main lobe throughout a substantially extended DOF. We showed both theoretically and experimentally the generation and propagation of the DRiP point-spread function (DRiP-PSF) of the imaging system. Lastly, we optimized the DRiP-PSF and successfully demonstrated diffraction-limited, depth-extended imaging of cellular structures.

2. Methods

2.1 System setup and configurations

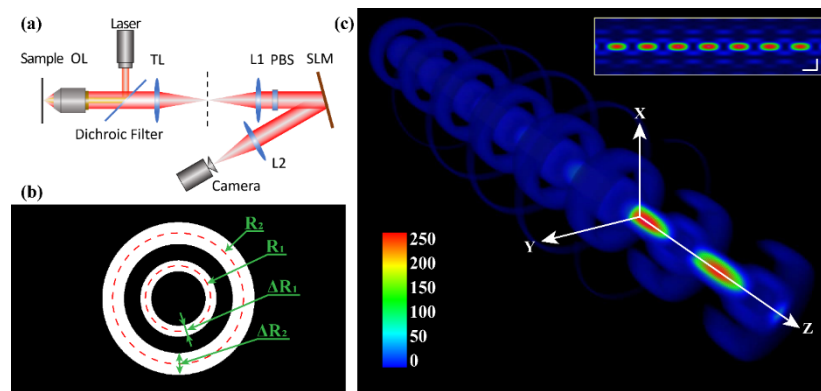


Fig. 1. System setup and configurations. (a) A schematic of the experimental setup. The objective lens (OL) and tube lens (TL) form an image of the sample at an intermediate image plane (black dashed line), which is relayed to the sCMOS camera by 4-f relay lenses (L1 and L2). The spatial-light modulator (SLM) situated at the Fourier plane of the relay lenses imparts DRiP phase modulation that converts the light into interfering Bessel-Gauss beams. PBS: polarizing beam-splitter. (b) Illustration of the DRiP modulation used on the SLM, composed of two concentric rings with finite thicknesses ΔR_1 and ΔR_2 . The dashed circles represent the average radii R_1 and R_2 . (c) Perspective view of a simulated 3D DRiP beam. The inset shows the cross-sectional x - z view of the beam. Scale bars: 400 nm.

The imaging system used in the study is shown in Fig. 1(a). The microscope (Nikon Eclipse Ti-U) utilized a 100x, 1.45 NA oil-immersion objective lens (CFI-PLAN Apo Lambda, Nikon) mounted on a piezo actuator (Mad City Labs), which controlled the axial position of the objective. The stage of the samples was controlled by a nano-positioning system (Applied Scientific Instrumentation). The samples were illuminated with a 647-nm fiber laser (MPB)

and the corresponding emitted fluorescence (peaked around 680 nm) was collected using a dichroic mirror (T660lpxr, Chroma) and an emission filter (ET700/75, Chroma). The intermediate image plane was imaged by a 4-f system ($f = 200$ mm) in the detection pathway, with a spatial-light modulator (SLM, PLUTO-VIS, Holoeye) placed at the Fourier plane. The images were recorded on a scientific complementary metal-oxide-semiconductor (sCMOS) camera (Andor Zyla 4.2 Plus).

In practice, Bessel beams can be generated by propagating a Gaussian beam through an axicon lens or a narrow annular aperture at the Fourier plane [3]. In this work, the DRiP modulation was obtained by creating two concentric annular apertures on the SLM with average radii ($R_1 = 1500$ μm and $R_2 = 3000$ μm) as illustrated in Fig. 1(b). Each annular aperture on the SLM is a Bessel-Gauss approximation using finite thickness ($\Delta R_1 = 500$ μm and $\Delta R_2 = 1000$ μm) to resemble the ideal Bessel beam solution without compromising its axial extent [18,34]. The radii and thicknesses of the two annuli were determined based on screening varying SLM phase patterns for an optimized DRiP beam performance, including the main lobe width, the ratio between the main and side lobes, the axial extent, as well as the photon efficiency provided by the finite thicknesses.

2.2 Theory of the 3D DRiP waveform

An ideal Bessel beam solution to the scalar Helmholtz equation $\Delta\Phi + k^2\Phi = 0$, where k is the wavenumber and Φ is the wavefunction, can be described as $\Phi(\rho, \varphi, z) = A_0 e^{-ik_z z} J_n(k_\rho \rho) e^{\pm i n \varphi}$, where ρ , φ , and z are cylindrical coordinates, k_z and k_ρ are the longitudinal and lateral wavevectors ($k = \sqrt{k_z^2 + k_\rho^2}$), A_0 is the scale coefficient, J_n is an n -th order Bessel function. Using a narrow annular aperture in the Fourier plane, the zeroth-order Bessel beam $\Phi(\rho, z) = A_0 e^{-ik_z z} J_0(k_\rho \rho)$ can be considered as a composition of plane waves propagating on a cone [2], which opening angle is described as $\eta = \tan^{-1}(k_\rho / k_z) = \tan^{-1}(R / f)$, where R is the radius of the annulus and f is the focal length of the imaging lens. Thus, the DRiP beam can be described as $\Phi(\rho, z) = J_0(k_\rho \rho) \sum_j A_j e^{-ik z \cos \eta_j}$, representing the superposition of two coaxial Bessel beams, created using two concentric annular apertures of opening angles $\eta_j = \tan^{-1}(R_j / f)$, where j represents the constituent Bessel beams ($j = 1, 2$).

Considering the Bessel-Gauss approximation in practice, the superposition of the two beams in three dimensions are given as [34]:

$$\Phi(\rho, z) = \sum_{j=1,2} A_j \frac{w_0}{w(z)} \exp \left[-i \left(\left(k - \frac{k \sin^2 \eta_j}{2} \right) z - \tan^{-1} \left(\frac{z}{z_R} \right) \right) \right] \times J_0 \left[\frac{\rho k \sin \eta_j}{\frac{iz}{z_R} + 1} \right] \exp \left[\left(\frac{ik}{2R_c(z)} - \frac{1}{w^2(z)} \right) (\rho^2 + \sin^2 \eta_j z^2) \right] \quad (1)$$

where A_j is the amplitude, w_0 and $w(z)$ are the Gaussian beam widths at waist and at propagation distance z , respectively, and $w(z) = w_0 \sqrt{1 + \left(\frac{z}{z_R} \right)^2}$, and the beam curvature

$R_C(z) = z + \frac{z_R^2}{z}$, where z_R is the Rayleigh length of the Gaussian beam. Therefore, the 3D intensity pattern of the DRiP beam is described as $I(\rho, z) = |\Phi(\rho, z)|^2$ (Fig. 1(c)). The values of the parameters (effective in the object domain, considering 100x magnification) are $A_j = 1$; $w_0 = 9.68 \mu\text{m}$; $z_R = 433 \mu\text{m}$; $k = 9.24 \times 10^6 \text{ m}^{-1}$; $\eta_j = 0.0075$ ($j = 1$), 0.0150 ($j = 2$); $\rho \in \{0, 141.42\} \mu\text{m}$; $z \in \{-3, 3\} \mu\text{m}$. Notably, unlike a single Bessel beam, the interference of the two Bessel beams leads to a remarkable spatial sequence of alternating bright and dark regions along the axial dimension at a period $d = 2\lambda / |\cos\eta_1 - \cos\eta_2|$ [9,35]. In this study, to form an axially-uniform profile throughout the DOF, we developed an approach to creating two additional DRiP beams that were axially translated by $\pm d/2$, respectively, using opposing Fresnel propagation generated by the SLM. As a result, the final beam, computationally created by averaging the three DRiP beams in three dimensions, exhibited a uniform profile for imaging the entire DOF without missing axial ranges (detailed in Section 3).

2.3 Numerical modeling for the 3D DRiP-PSF

The wavefunction of the 3D propagation of a point emitter imaged at the intermediate image plane of a high-NA microscopy system can be described by the scalar diffraction theory [36]:

$$U_i(\mathbf{x}, \mathbf{p}) = \frac{M}{f_{obj}^2 \lambda^2} \exp\left[-\frac{iu}{4\sin^2\left(\frac{\alpha}{2}\right)}\right] \times \int_0^\alpha P(\theta) \exp\left[\frac{iu\sin^2\left(\frac{\theta}{2}\right)}{2\sin^2\left(\frac{\alpha}{2}\right)}\right] J_0\left[\frac{\sin(\theta)}{\sin(\alpha)}v\right] \sin(\theta) d\theta \quad (2)$$

where f_{obj} is the focal length of the objective lens, and J_0 is the zeroth-order Bessel function of the first kind. The variables v and u represent normalized radial and axial coordinates; the two variables are defined by $v = k \left[(x_1 - p_1)^2 + (x_2 - p_2)^2 \right]^{1/2} \sin(\alpha)$ and $u = 4kp_3 \sin^2(\alpha/2)$; $\mathbf{p} = (p_1, p_2, p_3)$ is the position for a point source in a volume in the object domain; $\mathbf{x} = (x_1, x_2)$ represents the Cartesian coordinates on the intermediate image plane; M is the magnification of the objective lens; the half-angle of the NA is $\alpha = \sin^{-1}(NA/n)$; the wavenumber $k = 2\pi n / \lambda$ were calculated using the wavelength λ and the refractive index n of the immersion medium. For Abbe-sine corrected objectives, the apodization function of the microscope $P(\theta) = \cos(\theta)^{1/2} (1 + \cos(\theta))$ was used.

Next, the fluorescence emission can be modulated into Bessel beams using the 4-f imaging system as shown in Fig. 1(a). The spatial modulation of annular apertures in the Fourier plane is described as $\psi(r, \theta) = 1$ when $r \in \left[R_1 - \frac{\Delta R_1}{2}, R_1 + \frac{\Delta R_1}{2} \right]$ or $\left[R_2 - \frac{\Delta R_2}{2}, R_2 + \frac{\Delta R_2}{2} \right]$, and $\psi(r, \theta) = 0$ elsewhere, where (r, θ) are polar coordinates on the Fourier plane. The light propagation through the 4-f system can be described in a sequence of Fourier transform ($\mathcal{F}\{\}$), spatial modulation on the Fourier plane ($\psi(r, \theta)$), and inverse

Fourier transform ($\mathcal{F}^{-1}\{\}$). Thus, the final wavefunction on the camera sensor can be described as:

$$U_c(\mathbf{x}', \mathbf{p}) = \mathcal{F}^{-1}\{\mathcal{F}[U_i(\mathbf{x}, \mathbf{p})] \times \psi(r, \theta)\} \quad (3)$$

where $\mathbf{x}' = (x'_1, x'_2)$ represents the Cartesian coordinates on the camera sensor. The 3D PSF of the system for a point emitter can thus be described as $PSF(\mathbf{x}', \mathbf{p}) = |U_c(\mathbf{x}', \mathbf{p})|^2$. In this study, we utilized the above numerical model for simulating the propagation of the 3D DRiP-PSF in a high-resolution imaging system, which results agreed well with the experimental results (detailed in Section 3).

3. Results

3.1 Characterization of the DRiP-PSF

To characterize the 3D PSF of the imaging system, we first used sub-diffraction-limit 200-nm fluorescent beads as point emitters and recorded their images at different axial positions (Fig. 2). We compared the DRiP-PSF with the standard Gaussian PSF (GAU, or Airy disk, to be exact) and the Bessel PSFs generated with each individual annulus (represented as inner-ring (IR) or outer-ring (OR) PSFs). We noted three main features. First, as the sample was translated in z , the standard Gaussian PSF, recorded without phase modulation on the SLM, became significantly expanded due to diffraction beyond 0.5-1 μm from the focal plane (Fig. 2(a)). In contrast, the DRiP-PSF maintains a largely non-diffracting profile at a diffraction-limited FWHM of 250-300 nm over a $>4\text{-}\mu\text{m}$ range, showing $>4\text{-}5 \times$ improvement in the DOF (Fig. 2(a)-(c)). Secondly, the extended lateral profiles of both the IR and OR-PSFs induced stronger background compared to the DRiP-PSF (Fig. 2(a)). The interference of the two Bessel beams in the DRiP-PSF substantially suppressed the side lobes, exhibiting $>2\text{-}3 \times$ improvement in the ratio between the main lobe and the first side lobe. In addition, the DRiP-PSF showed a slightly narrower beam profile compared to the IR-PSF and a further extended DOF compared to the OR-PSF (Fig. 2(b),(c)), consistent with the theoretical prediction for Bessel beams generated with annular apertures of different opening angles. It should be noted that the FWHM values were obtained using Gaussian fitting of the main lobes of each PSF, which were affected by the lower peak-to-background ratio in the experimental results, especially for the OR-PSF. Theoretically, the main lobe width of a Bessel beam could reach the sub-diffraction limit compared to that of the corresponding Gaussian beam [37] (e.g. the OR-PSF in Fig. 2(d)-(f)). However, in practice, the experimental OR-PSF was broadened due to the fluorescent signal and stronger background (Fig. 2(b),(c)). Thirdly, the bright and dark regions alternating along the axial dimension in the DRiP-PSF were clearly noticed, leading to variations of both main lobe intensity and lateral size. The spacing between the two dark regions was measured to be 1.20 μm , compared to the theoretical value $d = 2\lambda / |\cos\eta_1 - \cos\eta_2| = 1.61 \mu\text{m}$. The deviation is mainly because the exact Bessel function used in the theoretical model (Section 2.2) overlooks the practical Bessel-Gauss beams generated in the imaging system. In contrast, the numerical simulation (Section 2.3) considering this approximation agreed well with the experimental measurements (Fig. 2(d)-(f)).

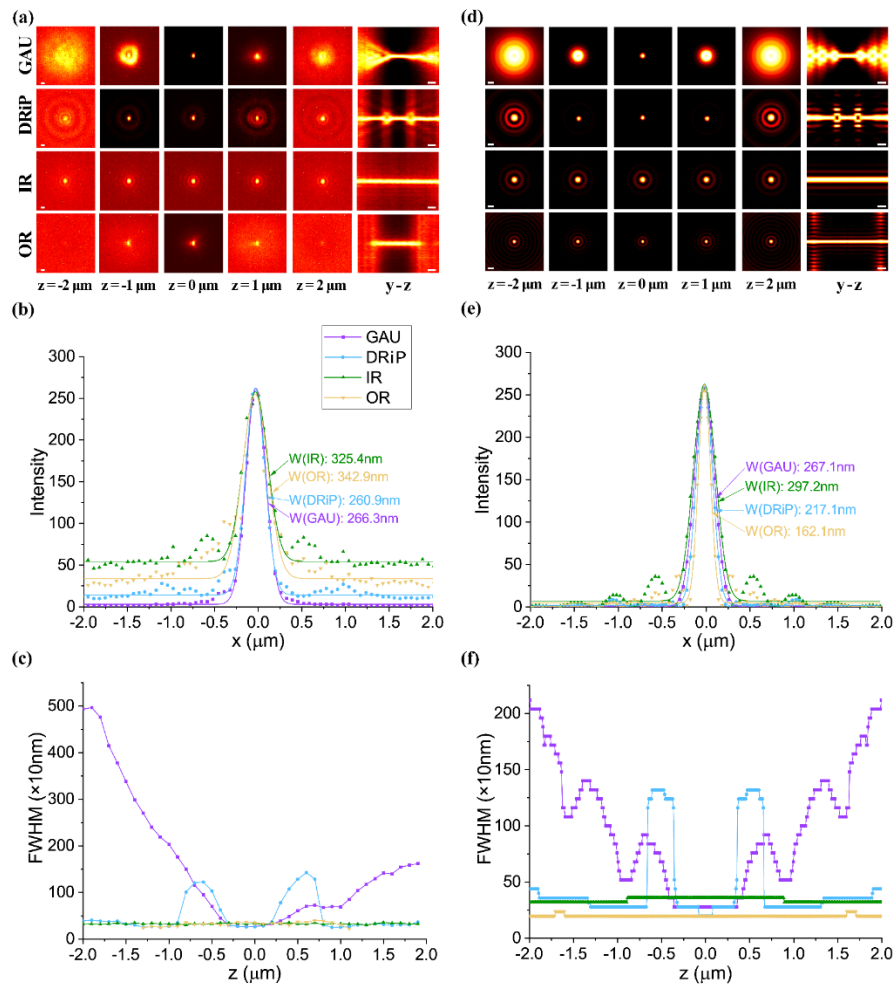


Fig. 2. Double-ring phase (DRiP) modulated point-spread function (DRiP-PSF). Both the experimental (left column, a-c) and numerical (right column, d-f) results were demonstrated. (a,d) x-y and y-z cross-sectional images of the Gaussian, DRiP, IR, and OR-PSFs, recorded as images of 200-nm fluorescent microspheres at several axial positions over a 4-μm z-range. The OR-PSF exhibited a shorter DOF in the experimental y-z view in (a). (b,e) Cross-sectional profiles of the PSFs at the focal plane (dotted lines). The FWHM values were determined by Gaussian-fitting of the main lobes (solid lines). (c,f) The FWHM values of the PSFs at varying axial positions over a 4-μm range. Scale bars: 400 nm.

It should also be noted that the photon efficiency of the current DRiP design is measured as 39.0%, compared to the theoretical value of 43.5%. The deviation from the theory is mainly because the theoretical model considered uniform distribution of photons on the pupil, which is practically Gaussian-distributed. Numerical simulations on the performance of the DRiP PSF as a function of double-ring parameters have been demonstrated in Fig. 5 in Appendix 1.

3.2 Creating axially-uniform DRiP-PSF

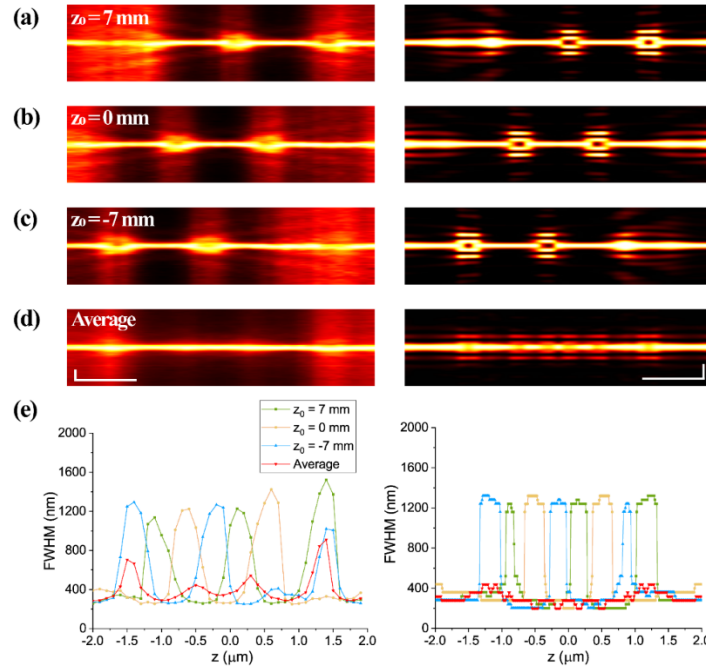


Fig. 3. Axially-uniform DRiP-PSF. Both the experimental (left column) and numerical (right column) results were demonstrated. (a-c) x - z images of positively translated ($z_0 = 7$ mm), original ($z_0 = 0$ mm), and negatively translated ($z_0 = -7$ mm) DRiP-PSFs. (d) x - z image of the average of the three DRiP-PSFs in (a-c). (e) The FWHM values of the cross-sectional profiles of the PSFs at varying axial positions over a 4-μm range, showing the compensation of the alternating patterns in the original and translated DRiP-PSFs and the more uniform profile in the averaged DRiP-PSF. Scale bars: 800 nm.

The axially alternating pattern of the main lobe of the DRiP-PSF leads to missing axial information in those dark regions. To address this limitation, we introduced two additional DRiP beams, axially translated in opposing directions by applying two corresponding phase masks of Fresnel propagation using the SLM (Fig. 3). The bright and dark regions of the original DRiP-PSF can thus be compensated by the two oppositely translated beams. Practically, the corresponding Fresnel phase pattern used on the SLM is described as $\Lambda = \exp(i2\pi\nu_z z_0)$, where the axial spatial frequency ν_z , represented as a function of the lateral spatial frequencies (i.e. Cartesian coordinates on the Fourier plane) (ν_x, ν_y) can be

described as $\nu_z(\nu_x, \nu_y) = \sqrt{\max\left\{0, \frac{1}{\lambda^2} - \nu_x^2 - \nu_y^2\right\}}$ [38]. Such phase pattern allows the incident

beam to propagate by z_0 after Fourier transform on the camera plane, which is effectively z_0 / M^2 in the object domain. The distance of translation could first be estimated using the experimentally measured spacing between the dark regions, i.e. $\pm d / 2 = \pm 0.6$ μm. We then adjusted about this predicted value and identified $z_0 = \pm 7$ mm, i.e. ± 0.7 μm in the object domain, so that the original DRiP beam ($z_0 = 0$) could be optimally compensated (Fig. 3(a)-(c)). Next, we computationally averaged the three DRiP beams in three dimensions, which exhibited an axially-uniform DRiP-PSF, maintaining a high resolution of the main lobe throughout a substantially extended DOF over > 4 μm (Fig. 3(d),(e)). By removing the

alternating broadening, this method makes the DRiP PSF practical for imaging. The use of the SLM allows for automatic creation and acquisition of the translated PSFs and generation of the axially-uniform DRiP-PSF in a timely manner up to 60 Hz without the need for any mechanical scanning. In addition, the numerical simulation using the Fresnel propagation agreed well with the experimental measurements (Fig. 3).

3.3 Imaging cells using the axially-uniform DRiP-PSF

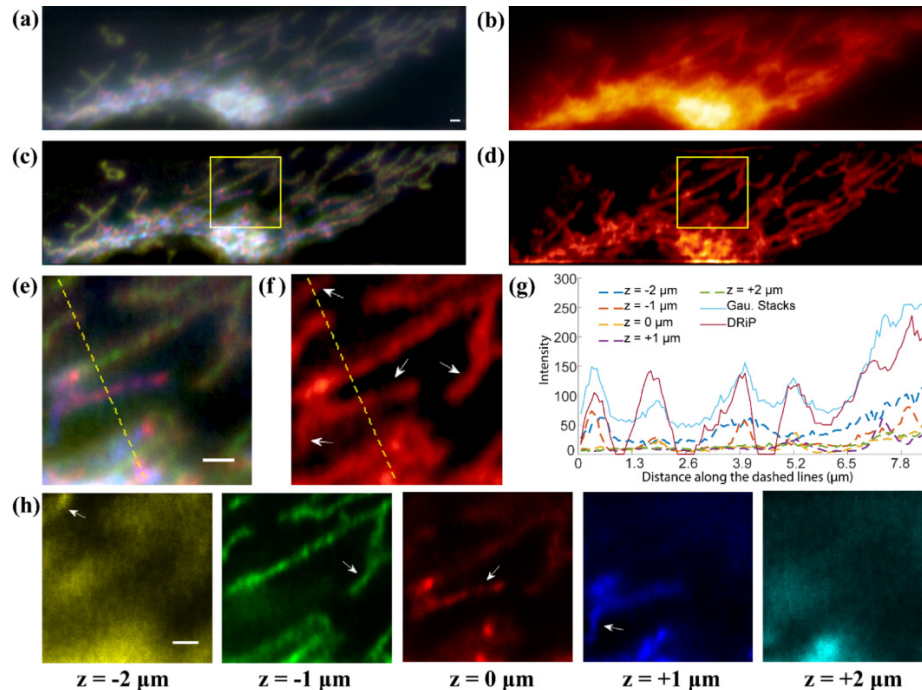


Fig. 4. Imaging mitochondria in cells using the axially-uniform DRiP-PSF. (a,b) Immunofluorescence images of mitochondria in a HeLa cell taken with the standard Gaussian (a) and DRiP (b) PSFs. (a) shows a stack of five Gaussian images at a step size of 1 μm over a 4- μm range. The depth information is color-coded according to (h). (c,d) The corresponding deconvolved images of (a,b), respectively. (e,f) Zoomed-in images of the boxed regions in (c,d), respectively. White arrows indicate the mitochondrial structures observed across an axial range of several micrometers by the DRiP-PSF, compared to those observed across several Gaussian stacks in (h). (g) Cross-sectional profiles along the dashed lines in (e,f). The image using the DRiP-PSF exhibited structural features across all z -stacks. (h) Individual z -stack images taken with the Gaussian PSF at $z = -2, -1, 0, 1, 2 \mu\text{m}$. White arrows indicate the corresponding mitochondrial structures observed across z -stacks using the Gaussian PSF, compared to (f). Scale bars, 1.3 μm .

Finally, we imaged immune-labelled mitochondria in mammalian cells using the axially-uniform DRiP-PSF and compared with conventional images taken using the Gaussian PSF without any modulation on the SLM (Fig. 4(a),(b)). Protocols for sample preparation were detailed in Appendix 2. For better visualization without epi-fluorescent background, similar comparison was also made between the corresponding deconvolved images using the experimental Gaussian and DRiP-PSFs, respectively (Fig. 4(c),(d)). Due to the limited DOF, the Gaussian images were recorded at a step size of 1 μm over 5 layers and stacked with different colors for comparison (Fig. 4(a),(c)). Remarkably, the sub-micrometer mitochondrial structures spanning a $\sim 4\text{-}\mu\text{m}$ axial range were clearly observed using the DRiP-PSF (Fig. 4(e)-(h)). The DRiP images not only maintained a high resolution over an extended range without the need for any sample or focal-plane scanning, but also captured

mitochondria that were completely undetectable in the conventional images due to diffraction of the Gaussian PSF (Fig. 4(g),(h)). The cell imaging results including the resolution, DOF and image contrast were consistent with the DRiP-PSF measurement (Figs. 2 and 3). The high-controllability of the DRiP waveform using the SLM, or other faster devices like deformable mirrors or digital micromirror device (DMD), allows for further optimization to visualize many other types of cellular structures that expand across a large volume in cells.

4. Conclusion

In this work, we have developed a DRiP method for depth-extended, high-resolution fluorescence microscopy. Using two interfering Bessel beams, the method not only maintains the non-diffracting property of Bessel beams, but also effectively suppresses the Bessel side lobes, substantially improving image contrast and resolution. Compared to conventional wide-field microscopy, the DRiP-PSF exhibits a diffraction-limited FWHM value of ~ 300 nm with four- to five-fold improvement of the DOF, allowing for imaging across a significant volume of whole cells without the need for scanning. The method represents a new method for fast projection of whole-cell dynamics for wide-field microscopy. Beyond wide-field microscopy, the method can be extended to various types of imaging modalities, such as particle tracking, light-sheet microscopy and one or two-photon microscopy. Furthermore, the DRiP method can be realized by implementing a fabricated double-annulus mask to the back pupil of the objective (i.e. the Fourier plane), advancing the method as a plug-in device compatible with most commercial optical microscopes. Transforming conventional Bessel beams, the method can also be used for optical manipulation, micro-machining, as well as generation of non-optical waveforms such as electron beams, acoustic and plasmonic waves.

Appendix 1

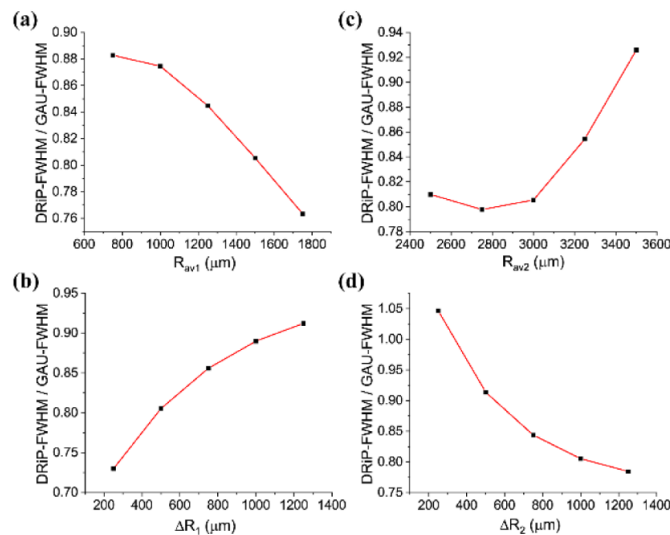


Fig. 5. Performance of the DRiP PSF as a function of double-ring parameters. (a) an increase in the radius of the inner ring, while maintaining all other parameters, will include more high spatial frequencies, thus leading to a decrease in the beam width; (b) an increase in the thickness of the inner ring causes the DRiP PSF close to a Gaussian; (c) an increase in the radius of the outer ring will continue to decrease the beam width at the beginning until the outer ring exceeds the pupil size of the objective, when gaining only low spatial frequencies leads to an increase in the beam width; (d) an increase in the thickness of the outer ring introduces more high spatial frequencies, leading to a decrease in the beam width.

Appendix 2

For sample preparation, HeLa cells were obtained from the American Type Culture Collection (ATCC), maintained in $1\times$ Minimum Essential Medium (MEM) (Corning CellGro) with 10% fetal bovine serum (FBS) (Atlanta Biologicals) and 50 $\mu\text{g/ml}$ gentamycin (Amresco), and incubated at 37°C with 5% CO_2 . The cells were plated on a 35 mm^2 glass-bottom plate (MatTek), incubated at 37°C for 16 hours, and fixed with 4% (vol/vol) formaldehyde (Electron Microscopy Sciences) prepared in phosphate buffered saline (PBS) for 10 mins at 37°C . The cells were then blocked and permeabilized with blocking and antibody dilution buffer (1% (vol/vol) bovine serum albumin (BSA) (Santa Cruz Biotechnologies) and 0.25% (vol/vol) Triton X-100 prepared in PBS) for 1 hour at room temperature. The cells were then incubated with the mitochondrial marker primary antibody mouse anti-Tom20 (Santa Cruz Biotechnologies F10, SC-17764), at 1 $\mu\text{g/ml}$ in blocking and antibody dilution buffer for 2 hours while gently shaking at room temperature. The cells were then washed 3 times with PBS for 5 mins each. Secondary antibody (AlexaFluor 647-conjugated AffiniPure Goat Anti-Mouse IgG, 1 mg/ml , Jackson ImmunoResearch) was diluted 1:1000 in 1% BSA in PBS and incubated with gentle shaking for 1 hour at room temperature. The cells were washed 3 times with PBS for 5 mins. The cells were placed in imaging buffer (20 mM HEPES pH 7.4, 135 mM NaCl, 5 mM KCl, 1 mM MgCl_2 , 1.8 mM CaCl_2 , 5.6 mM glucose) before imaging.

Funding

National Institutes of Health (1R35GM124846); National Science Foundation (CBET1604565 and EFMA1830941).

Acknowledgments

We acknowledge the support of the NSF-CBET Biophotonics program, the NSF-EFMA program, and the NIH-NIGMS MIRA program.

Disclosures

The authors declare that there are no conflicts of interest related to this article.

References

1. J. Durnin, "Exact solutions for nondiffracting beams I The scalar theory," *J. Opt. Soc. Am. A* **4**(4), 651 (1987).
2. J. Durnin, J. Miceli, Jr., and J. H. Eberly, "Diffraction-free beams," *Phys. Rev. Lett.* **58**(15), 1499–1501 (1987).
3. D. McGloin and K. Dholakia, "Bessel beams: Diffraction in a new light," *Contemp. Phys.* **46**(1), 15–28 (2005).
4. I. Kaminer, R. Bekenstein, J. Nemirovsky, and M. Segev, "Nondiffracting accelerating wave packets of Maxwell's equations," *Phys. Rev. Lett.* **108**(16), 163901 (2012).
5. F. Courvoisier, A. Mathis, L. Froehly, R. Giust, L. Furfaro, P. A. Lacourt, M. Jacquot, and J. M. Dudley, "Sending femtosecond pulses in circles: highly nonparaxial accelerating beams," *Opt. Lett.* **37**(10), 1736–1738 (2012).
6. P. Zhang, Y. Hu, T. Li, D. Cannan, X. Yin, R. Morandotti, Z. Chen, and X. Zhang, "Nonparaxial Mathieu and Weber accelerating beams," *Phys. Rev. Lett.* **109**(19), 193901 (2012).
7. C. Vetter, T. Eichelkraut, M. Ornigotti, and A. Szameit, "Generalized radially self-accelerating helicon beams," *Phys. Rev. Lett.* **113**(18), 183901 (2014).
8. V. Garcés-Chávez, D. McGloin, H. Melville, W. Sibbett, and K. Dholakia, "Simultaneous micromanipulation in multiple planes using a self-reconstructing light beam," *Nature* **419**(6903), 145–147 (2002).
9. D. B. Ruffner and D. G. Grier, "Optical conveyors: a class of active tractor beams," *Phys. Rev. Lett.* **109**(16), 163903 (2012).
10. M. K. Bhuyan, F. Courvoisier, P. A. Lacourt, M. Jacquot, R. Salut, L. Furfaro, and J. M. Dudley, "High aspect ratio nanochannel machining using single shot femtosecond Bessel beams," *Appl. Phys. Lett.* **97**(8), 081102 (2010).
11. J. Arlt, V. Garcés-Chavez, W. Sibbett, and K. Dholakia, "Optical micromanipulation using a Bessel light beam," *Opt. Commun.* **197**(4-6), 239–245 (2001).
12. A. Chong, W. H. Renninger, D. N. Christodoulides, and F. W. Wise, "Airy-Bessel wave packets as versatile linear light bullets," *Nat. Photonics* **4**(2), 103–106 (2010).
13. T. Wulle and S. Herminghaus, "Nonlinear optics of Bessel beams," *Phys. Rev. Lett.* **70**(10), 1401–1404 (1993).

14. V. Grillo, E. Karimi, G. C. Gazzadi, S. Frabboni, M. R. Dennis, and R. W. Boyd, "Generation of nondiffracting electron Bessel beams," *Phys. Rev. X* **4**(1), 011013 (2014).
15. Y. Monnai, D. Jahn, W. Withayachumnankul, M. Koch, and H. Shinoda, "Terahertz plasmonic Bessel beamformer," *Appl. Phys. Lett.* **106**(2), 021101 (2015).
16. Y. Tian, Q. Wei, Y. Cheng, Z. Xu, and X. Liu, "Broadband manipulation of acoustic wavefronts by pentamode metasurface," *Appl. Phys. Lett.* **107**(22), 221906 (2015).
17. J. Harris, V. Grillo, E. Mafakheri, G. C. Gazzadi, S. Frabboni, R. W. Boyd, and E. Karimi, "Structured quantum waves," *Nat. Phys.* **11**(8), 629–634 (2015).
18. T. A. Planchon, L. Gao, D. E. Milkie, M. W. Davidson, J. A. Galbraith, C. G. Galbraith, and E. Betzig, "Rapid three-dimensional isotropic imaging of living cells using Bessel beam plane illumination," *Nat. Methods* **8**(5), 417–423 (2011).
19. F. O. Fahrbach, P. Simon, and A. Rohrbach, "Microscopy with self-reconstructing beams," *Nat. Photonics* **4**(11), 780–785 (2010).
20. L. Gao, L. Shao, C. D. Higgins, J. S. Poulton, M. Peifer, M. W. Davidson, X. Wu, B. Goldstein, and E. Betzig, "Noninvasive imaging beyond the diffraction limit of 3D dynamics in thickly fluorescent specimens," *Cell* **151**(6), 1370–1385 (2012).
21. F. O. Fahrbach and A. Rohrbach, "Propagation stability of self-reconstructing Bessel beams enables contrast-enhanced imaging in thick media," *Nat. Commun.* **3**(1), 632 (2012).
22. Y. Chen and J. T. C. Liu, "Characterizing the beam steering and distortion of Gaussian and Bessel beams focused in tissues with microscopic heterogeneities," *Biomed. Opt. Express* **6**(4), 1318–1330 (2015).
23. R. Lu, W. Sun, Y. Liang, A. Kerlin, J. Bierfeld, J. D. Seelig, D. E. Wilson, B. Scholl, B. Mohar, M. Tanimoto, M. Koyama, D. Fitzpatrick, M. B. Orger, and N. Ji, "Video-rate volumetric functional imaging of the brain at synaptic resolution," *Nat. Neurosci.* **20**(4), 620–628 (2017).
24. P. Zhang, P. M. Goodwin, and J. H. Werner, "Fast, super resolution imaging via Bessel-beam stimulated emission depletion microscopy," *Opt. Express* **22**(10), 12398–12409 (2014).
25. G. Thériault, M. Cottet, A. Castonguay, N. McCarthy, and Y. De Koninck, "Extended two-photon microscopy in live samples with Bessel beams: steadier focus, faster volume scans, and simpler stereoscopic imaging," *Front. Cell. Neurosci.* **8**, 139 (2014).
26. A. Song, A. S. Charles, S. A. Koay, J. L. Gauthier, S. Y. Thiberge, J. W. Pillow, and D. W. Tank, "Volumetric two-photon imaging of neurons using stereoscopy (vTwINS)," *Nat. Methods* **14**(4), 420–426 (2017).
27. J. Durnin, J. J. Miceli, Jr., and J. H. Eberly, "Comparison of Bessel and Gaussian beams," *Opt. Lett.* **13**(2), 79 (1988).
28. B. C. Chen, W. R. Legant, K. Wang, L. Shao, D. E. Milkie, M. W. Davidson, C. Janetopoulos, X. S. Wu, J. A. Hammer 3rd, Z. Liu, B. P. English, Y. Mimori-Kiyosue, D. P. Romero, A. T. Ritter, J. Lippincott-Schwartz, L. Fritz-Laylin, R. D. Mullins, D. M. Mitchell, J. N. Bembenek, A. C. Reymann, R. Böhme, S. W. Grill, J. T. Wang, G. Seydoux, U. S. Tulu, D. P. Kiehart, and E. Betzig, "Lattice light-sheet microscopy: imaging molecules to embryos at high spatiotemporal resolution," *Science* **346**(6208), 1257998 (2014).
29. M. Zhao, H. Zhang, Y. Li, A. Ashok, R. Liang, W. Zhou, and L. Peng, "Cellular imaging of deep organ using two-photon Bessel light-sheet nonlinear structured illumination microscopy," *Biomed. Opt. Express* **5**(5), 1296–1308 (2014).
30. F. O. Fahrbach and A. Rohrbach, "A line scanned light-sheet microscope with phase shaped self-reconstructing beams," *Opt. Express* **18**(23), 24229–24244 (2010).
31. P. Zhang, M. E. Phipps, P. M. Goodwin, and J. H. Werner, "Confocal line scanning of a Bessel beam for fast 3D imaging," *Opt. Lett.* **39**(12), 3682–3685 (2014).
32. I. Golub, B. Chebbi, and J. Golub, "Toward the optical "magic carpet": reducing the divergence of a light sheet below the diffraction limit," *Opt. Lett.* **40**(21), 5121–5124 (2015).
33. J. Lin, J. Dellinger, P. Genevet, B. Cluzel, F. de Fornel, and F. Capasso, "Cosine-Gauss plasmon beam: a localized long-range nondiffracting surface wave," *Phys. Rev. Lett.* **109**(9), 093904 (2012).
34. F. Gori, G. Guattari, and C. Padovani, "Bessel-Gauss beams," *Opt. Commun.* **64**(6), 491–495 (1987).
35. G. Antonacci, G. D. Domenico, S. Silvestri, E. DelRe, and G. Ruocco, "Diffraction-free light droplets for axially-resolved volume imaging," *Sci. Rep.* **7**(1), 17 (2017).
36. M. Gu, *Advanced Optical Imaging Theory* (Springer, 2000).
37. C. Snoeink and S. Wereley, "Single-image far-field subdiffraction limit imaging with axicon," *Opt. Lett.* **38**(5), 625–627 (2013).
38. J. Goodman, *Introduction to Fourier Optics*, in 3rd ed. (Roberts and Company, 2005), pp. 127–172.